THE JOURNAL OF PHYSICAL CHEMISTRY A

 VOLUME 109, NUMBER 37, SEPTEMBER 22, 2005

ARTICLES

Ground and Excited State Dissociation Dynamics of Ionized 1,1-Difluoroethene

E. Gridelet,† D. Dehareng,‡ R. Locht,† A. J. Lorquet,† J. C. Lorquet,† and B. Leyh*,†

Department of Chemistry, Molecular Dynamics Laboratory, Building B6c, and Centre for Protein Engineering, Building B6a, University of Liège, B-4000 SART-TILMAN, Belgium

Received: March 25, 2005; In Final Form: July 25, 2005

The kinetic energy release distributions (KERDs) for the fluorine atom loss from the 1,1-difluoroethene cation have been recorded with two spectrometers in two different energy ranges. A first experiment uses dissociative photoionization with the He(I) and Ne(I) resonance lines, providing the ions with a broad internal energy range, up to 7 eV above the dissociation threshold. The second experiment samples the metastable range, and the average ion internal energy is limited to about 0.2 eV above the threshold. In both energy domains, KERDs are found to be bimodal. Each component has been analyzed by the maximum entropy method. The narrow, low kinetic energy components display for both experiments the characteristics of a statistical, simple bond cleavage reaction: constraint equal to the square root of the fragment kinetic energy and ergodicity index higher than 90%. Furthermore, this component is satisfactorily accounted for in the metastable time scale by the orbiting transition state theory. Potential energy surfaces corresponding to the five lowest electronic states of the dissociating 1,1-$C_2H_2F_2^+$ ion have been investigated by ab initio calculations at various levels. The equilibrium geometry of these states, their dissociation energies, and their vibrational wavenumbers have been calculated, and a few conical intersections between these surfaces have been identified. It comes out that the ionic ground state $\tilde{X}^2B_1$ is adiabatically correlated with the lowest dissociation asymptote. Its potential energy curve increases in a monotonic way along the reaction coordinate, giving rise to the narrow KERD component. Two states embedded in the third photoelectron band ($\tilde{B}^2A_1$ at 15.95 eV and $\tilde{C}^2B_2$ at 16.17 eV) also correlate with the lowest asymptote at 14.24 eV. We suggest that their repulsive behavior along the reaction coordinate be responsible for the KERD high kinetic energy contribution.

I. Introduction

The loss of a fluorine atom from the three isomers of the difluoroethene cation (1,1-$C_2H_2F_2^+$, *cis*-1,2-$C_2H_2F_2^+$, and *trans*-1,2-$C_2H_2F_2^+$) has been investigated for a long time. Lifshitz and Long suggested in 1965 a nonstatistical dynamics in this fragmentation.[1] Other investigations support this hypothesis. In 1973, Reinke et al., who recorded the photoionization yield curve for 1,1-difluoroethene dissociation,[2] observed a strong intensity increase at 15.73 eV. In 1974, Frey's photoelectron−photoion coincidence (PEPICO) measurements highlighted a bimodal behavior in the breakdown diagram of 1,1-$C_2H_2F_2^+$ for the F loss channel, with a minimum around 15.4 eV. In addition, his time-of-flight (TOF) spectra revealed a broadening of the kinetic energy distribution starting at the same energy.[3] More recently, in 1999, 1,1-difluoroethene was studied with a threshold-PEPICO technique by Güthe and al., who confirmed the minimum at 15.4 eV in the breakdown diagram.[4] They observed a rapid increase in the kinetic energy release upon an

* Corresponding author. E-mail: Bernard.Leyh@ulg.ac.be. Phone: ++32-4-3663425. Fax: ++32-4-3663413.
† Molecular Dynamics Laboratory.
‡ Centre for Protein Engineering.

10.1021/jp051542b CCC: $30.25
Published on Web 08/30/2005

internal energy increase up to 16 eV photon energy, followed by some kind of a plateau and then by a further rapid increase starting at $h\nu \approx 18$ eV. This latter regime was interpreted as resulting from consecutive reactions, for example, further F or H loss from $C_2H_2F^+$, that become possible in this energy range.[4]

The common dissociation pattern of the three $C_2H_2F_2^+$ isomers has been highlighted experimentally[5] and confirmed by now dated quantum chemical calculations.[6] The latter led to the conclusion that the lowest dissociation channel requires an isomerization from the *trans*-1,2 to the *cis*-1,2 structure and then to 1,1-difluoroethene before the loss of a fluorine atom takes place. Furthermore, both 1,2-difluoroethene isomers also show a minimum in their breakdown diagram near 15 eV.[7,8] As a matter of fact, the occurrence of a specific fragmentation from an excited electronic state has been suggested in many reactions involving the loss of a fluorine atom from a molecular cation: $C_2H_3F^+$,[9−11] CF_3Cl^+,[12,13] $C_2F_6^+$,[14−16] CH_3F^+,[17,18] CF_4^+,[13,19] $C_3F_8^+$,[14] and $C_4F_{10}^+$.[14]

To analyze in more detail the supposed nonergodic process taking place in 1,1-$C_2H_2F_2^+$, we investigate in the present paper the kinetic energy release distributions (KERDs) associated with the F loss dissociation

$$1,1\text{-}C_2H_2F_2^+ \rightarrow C_2H_2F^+ + F \qquad (1.1)$$

Two internal energy domains are considered: a narrow, low internal energy range, corresponding to the metastable window, and a wider, high energy range, reached by dissociative photoionization. The KERDs are then analyzed by the maximum entropy method [20,21] that leads to a quantitative estimation of the degree of ergodicity of the reaction and is therefore particularly suited to detect nonstatistical situations.

This paper is organized as follows. Section II describes the experimental procedures. The maximum entropy method is presented briefly in section III together with the ab initio calculations necessary to compute the prior distribution. The results are described in section IV. Their analysis requires information about the potential energy surfaces: ab initio calculations are thus presented in section V. Section VI deals with the discussion of the experimental results based on the ab initio data. The main results are gathered in the concluding section VII.

II. Experiment

The kinetic energy release distribution, denoted as $P(\epsilon|E)$, is the probability of releasing a kinetic energy, ϵ, on the dissociation fragments if E is the excess energy with respect to the dissociation asymptote (located at 14.24 eV above the 1,1-$C_2H_2F_2$ vibrationless ground state[22]). Both spectrometers used to measure it in specific energy ranges have already been described in previous publications,[23−28] and only the most salient features are noted here.

A. Metastable Dissociations. The experimental setup used to sample the metastable energy range is a two-sector forward geometry instrument; that is, the electrostatic analyzer is followed by the magnet. Parent ions are produced upon electron impact in the spectrometer source and then accelerated by a voltage difference, V_{acc}. Scanning V_{acc}, with fixed electric and magnetic fields, one records a mass spectrum of parent ions dissociating to a given fragment ion in the first field free region of the spectrometer.[29−31] In this ion kinetic energy spectrum measured in the laboratory reference frame, mass peaks are broadened by the kinetic energy released during the fragmentation.

Then, KERDs are deduced from the experimental peak shape by a differentiation procedure followed by a change of variables from the laboratory to the center-of-mass reference frame.[32−34] In the case of low translational energy releases, a deconvolution step is included in the data handling in order to remove the broadening by the experimental apparatus function.[24] Because, in the present work, the ion translational energy in the direction of the spectrometer optical axis is around 7 keV with respect to the laboratory reference frame, whereas the peak width is only 50 eV, angular discrimination effects may be neglected in the treatment. Otherwise, they could be taken into account by a more elaborate procedure.[35−37]

1,1-Difluoroethene (commercially available from ABCR with 99% purity) was used without further purification**.** In the spectrometer source, the ionizing electron kinetic energy is equal to 70 eV and the ion current is set at 10 or 30 μA. The accelerating voltage, V_{acc}, is around 7 kV. The electrostatic analyzer exit slit (β-slit) width is adjusted to 0.25 mm to reach a translational energy resolution, $\Delta E/E$, of 10^{-3}.

Fragmentations taking place in the spectrometer first field free region occur in a given time window characterized by the entrance time, τ_1, into this region and by the exit time, τ_2, out of this region. Through the rate constant, $k(E)$, this time selection is equivalent to the selection of a relatively narrow energy range. Accordingly, the internal energy distribution of the parent ions is given by the product of a transmission function, that depends on the rate constant, and of the branching ratio, $R(E)$, corresponding to the selected dissociation channel (here, $C_2H_2F^+ + F$):

$$T(E) = A[\exp(-k(E)\tau_1) - \exp(-k(E)\tau_2)]R(E) \qquad (2.1)$$

where A is a normalization constant and $k(E)$ and $R(E)$ are taken from refs 38 and 4. In the present work, considering the uncertainties on the thermochemical threshold and on the rate constant, the average internal energy can be estimated to be lower than 0.3 eV. An average value of 0.17 eV has been adopted, on the basis of the appearance energy of ref 22. The width of $T(E)$ corresponds to a standard deviation of 0.07 eV. $T(E)$ corresponds therefore to an energy domain close to the reaction threshold.

It must be emphasized that no information is available for this reaction about quantum statistical fluctuations of the rate constant resulting from the fact that individual quantum eigenstates at a given energy, E, may not all decay with the same rate. The experimental data of ref 38 provide us only with an average $k(E)$ curve.

B. Photoionization/Retarding Field Analysis. This technique gives access to a more extended internal energy range of a few electronvolts. The sample, introduced by effusion in a reaction chamber, is ionized by photons emitted by a rare gas discharge lamp. The resonance lines Ne(I) (16.65−16.87 eV) and He(I) (21.21 eV) were used in the present case. Photoelectron spectra are recorded by a Lindau-type electron energy analyzer, and ions ($C_2H_2F_2^+$ or $C_2H_2F^+$) are analyzed by an ion retarding potential device, followed by a quadrupole mass spectrometer. The measurement principle is that only ions with enough kinetic energy are able to surmount the retarding potential barrier and are thus detected. Therefore, scanning the retarding potential while focusing on a given fragment ion whose kinetic energy is denoted ϵ_f, one gets a retarding curve, $I(\epsilon_f)$: its derivative leads then to the kinetic energy distribution. Taking into account the fact that the experimental device discriminates against high kinetic energies, the relationship between the

retarding curve and the ion translational energy distribution, $\tilde{P}^{f}(\epsilon_f)$, becomes

$$\tilde{P}^{f}(\epsilon_f) \propto \epsilon_f^{\mu} \frac{dI(\epsilon_f)}{d\epsilon_f} \tag{2.2}$$

where $\mu = 0.43 \pm 0.03$.[27] For every measurement, fragment ion and parent ion retarding curves have been recorded sequentially.

The internal energy distribution of $C_2H_2F_2^+$ is given by the He(I) or Ne(I) photoelectron spectrum multiplied by the branching ratio, $R(E)$, for the selected dissociation channel.[4] As the appearance energy for $C_2H_2F^+$ is equal to 14.24 eV,[22] the Ne(I) experiment explores an internal energy range up to 2.5 eV above the fragmentation asymptote and the He(I) measurement, up to 7 eV. The average internal energy, $\langle E \rangle$, is equal to 1.5 eV for Ne(I) and 3 eV for He(I).

In such retarding field experiments, the thermal energy of the parent ion provides a non-negligible contribution to the fragment kinetic energy and a deconvolution step is compulsory.[28] The velocities corresponding to the thermal motion [with the distribution $\tilde{P}^{T}(v)$] and to the kinetic energy released [with the distribution $\tilde{P}^{KER}(v)$] are vectorially added to give the observed fragment velocity [with the distribution $\tilde{P}^{f}(v)$]. For that reason, mathematically, the deconvolution equation must consider the velocity vectors and not the kinetic energies:

$$\tilde{P}^{f}(\vec{v}) = \tilde{P}^{T} * \tilde{P}^{KER}(\vec{v}) \tag{2.3}$$

where the transformation of variables is $v = |\vec{v}| = (2\epsilon_f/m_f)^{1/2}$.

The first step of our analysis is to obtain the thermal distribution, $\tilde{P}^{T}(\vec{v})$, by a fit of the parent ion retarding curve based on a Maxwell velocity distribution. We noticed only a small difference (about 15%) between the effective temperature found by this fit and the estimated ion source temperature.

To proceed further, we need a suitable analytical form for $\tilde{P}^{KER}(\vec{v})$. Note that $\vec{v}$ refers to the ionic fragment: its kinetic energy, ϵ_f, is related to the total kinetic energy released on both fragments, ϵ, by

$$\epsilon = m(C_2H_2F_2^{+}) \cdot \epsilon_f / m(F) \tag{2.4}$$

As we shall see in the next section, the maximum entropy formalism provides us with a suitable analytical form for $\tilde{P}(\epsilon)$ (eq 3.2) and thus for $\tilde{P}^{KER}(\vec{v})$. This form depends on Lagrange multipliers, which are obtained by fitting eq 2.3 to the experimental data. The subsequent procedure will be explained in section IV. Once these parameters have been obtained, the deconvoluted distribution, expressed in terms of either velocity or kinetic energy, can be easily calculated.

III. Maximum Entropy Method

A. Basic Equations. Consider a completely statistical dissociation at internal energy E. In such a case, all quantum states of the pair of fragments are equally probable. The corresponding kinetic energy release distribution is called the prior distribution and is simply given by the densities of states corresponding to the degrees of freedom of the pair of fragments:[20,21,39−41]

$$P^0(\epsilon|E) = N^0(E) \epsilon^{1/2} \rho_{int}(E - \epsilon) \tag{3.1}$$

$N^0(E)$ is a normalization factor, $\epsilon^{1/2}$ is the energy dependence of the three-dimensional density of states for the relative translation of the fragments, and ρ_{int} stands for the density of internal states of the dissociation fragments. Such a situation describes a complete sampling of the phase space available to the fragments at energy E.

In an actual situation, however, dynamical effects take place so that the system does not necessarily behave statistically. The maximum entropy formalism relates the deviations from statisticity to constraints, $A_r(\epsilon)$, that prevent the system from fully exploring the available phase space. The constrained KERD that corresponds to the largest entropy can be written as follows[21]

$$P(\epsilon|E) = P^0(\epsilon|E) \exp[-\lambda_0(E)] \prod_{r=1}^{n} \exp[-\lambda_r(E) A_r(\epsilon)] \tag{3.2}$$

where the parameter $\lambda_0(E)$ ensures normalization and $\lambda_r(E)$ designates the Lagrange parameter conjugated to the constraint, $A_r(\epsilon)$. Equation 3.2 can be shown to converge to an exact quantum mechanical expression of $P(\epsilon|E)$.[42]

In many situations, a single constraint ($n = 1$) is sufficient to account for the difference between the prior and the experimental distributions.[23,24,28,43−45] However, the fluorine loss from the 1,1-difluoroethene cation is a complex mechanism and, in the present work, this equation will be used in some instances with two or even three constraints ($n = 2$ or 3).

The nonstatistical character is quantified by the entropy deficiency, that is, by the always positive difference between the entropy of the prior distribution and that of the experimental one:

$$DS(E) = -\lambda_0(E) - \sum_r \lambda_r(E) \langle A_r(\epsilon) \rangle \tag{3.3}$$

DS(E) is related to the ergodicity index

$$F(E) = \exp[-DS(E)] \tag{3.4}$$

which gives an upper bound for the ratio of two phase space volumes: (i) the volume actually explored by the fragments and (ii) the available volume at energy E.[46]

An additional complication arises from the fact that the experimental distribution corresponds to a more or less wide internal energy range, so that $P(\epsilon|E)$ has to be averaged over the distribution $T(E)$ introduced in section II:

$$\tilde{P}(\epsilon) = \int_{\epsilon}^{\infty} P(\epsilon|E)\, T(E)\, dE \tag{3.5}$$

B. The Prior Distribution. The calculation of the prior distribution requires the knowledge of the density of states of the $C_2H_2F^+$ fragment. Ab initio calculations were carried out with the Gaussian system of programs.[47] To check the stability of the predictions, a sequence of calculations was carried out with basis sets of increasing size, ranging from 6-31G(d) or cc-pVDZ to 6-311++G(2df,2p).[48] The correlation was introduced, first by the density functional theory (B3LYP) and, in a second approach, by the quadratic configuration interaction with single and double excitations (QCISD) method.[48] For the signification of the quantum chemical acronyms, see ref 48. It is gratifying to note that the different methods give results that differ by 0.1 eV or less (except for the $^1A_1$ cyclic transition state discussed below).

The lowest energy was obtained for a singlet $^1A_1$ state in a symmetrical H_2CCF^+ geometry belonging to the C_{2v} point group. Its equilibrium position was taken as the origin of the energy scale. Another possible, less symmetrical $^1A'$ structure $HCCHF^+$ was found to give rise to an extremely shallow minimum when the calculations were carried out in a fairly small basis set [6-31G(d)]. However, the minimum vanished when

the basis set was increased and was replaced by a flat region of the potential energy surface, at an energy of about 1.07 eV (uncorrected for zero-point energy). This feature is a source of anharmonicity, which was taken into account in the calculation of the density of states reported below. The symmetrical $^1A_1$ three-membered cycle (with the fluorine bridging both carbon atoms, C_{2v} point group) was found to correspond to a saddle point. All calculations locate it about 1.75 eV above the deepest well, except the QCISD/6-31G(d) method, which provides a value of 1.55 eV. (Energy values of all stationary points have been corrected for the zero-point energy.)

The triplet $^3A''$ surface has a much more complicated shape. Two identical H_2CCF^+ minima were detected at 1.47 eV. They belong to the C_s point group, with a CCF angle equal to $+127°$ (or $-127°$), and are interconnected by two transition states. One of them ($^3A_2$) belongs to the C_{2v} point group and lies at an energy of 2.52 eV. The second saddle point is nonplanar and has C_s symmetry; its energy is 2.39 eV. Therefore, the existence of a two-dimensional double-well structure in the surface is a source of anharmonicity for two low energy vibrational normal modes. Still a third mode is anharmonic, because it connects the H_2CCF^+ and $HCCHF^+$ isomers via a nonplanar transition state located at an energy of 3.59 eV.

The $HCCHF^+$ $^3A''$ isomer has a planar C_s structure with two (in principle nonequivalent) minima. In one of them, the lone hydrogen is close to the other one; its energy is equal to 1.57 eV. In the other equilibrium geometry, it is close to the fluorine atom, and the energy is equal to 1.58 eV. However, the interconversion barrier is very low (less than 0.2 eV) and, hence, this isomer is highly fluxional. In addition, the nonplanar transition state at an energy of 3.59 eV reported above provides another source of anharmonicity.

The vibrational wavenumbers and rotational constants of the different isomers were calculated at the B3LYP/6-31G(d) level recommended by Scott and Radom[49] and were scaled according to their prescriptions. On the basis of these results, the rovibronic density of states of the $C_2H_2F^+$ fragment was calculated by the direct count method, using a Beyer−Swinehart routine[39,50] modified by us to take into account the anharmonicity detected in many oscillators. Rovibrational densities of states were calculated separately for the singlet state and for each of the two triplet isomers. The resulting energy-level density functions were then simply added to generate a final rovibronic function, which was then injected into eq 3.1. However, the energy gap between the singlet and triplet states is fairly large (of the order of 1.5 eV). Therefore, the total rovibronic energy-level density was found to be only slightly higher than the rovibrational function pertaining to the singlet state alone. Their ratio is equal to 1.08, 1.27, 1.35, and 1.53 at internal energies of 4, 5, 6, and 7 eV, respectively.

IV. Results

A. Metastable Internal Energy Range. The kinetic energy release distribution for 1,1-$C_2H_2F_2^+ \rightarrow C_2H_2F^+ + F$ measured in the metastable time window is displayed in Figure 1. The average kinetic energy release is equal to 0.073 ± 0.002 eV. A bimodal behavior is clearly seen, with a narrow low kinetic energy component and a wider higher kinetic energy component starting at $\epsilon \sim 0.05$ eV. The reproducibility has been tested with regard to both the experimental data and the data handling procedure (see the Experiment section). Starting from the hypothesis that a bimodal distribution results from the superposition of two phenomena characterized by different translational energy releases, the experimental KERD has been modeled as a sum of two contributions:

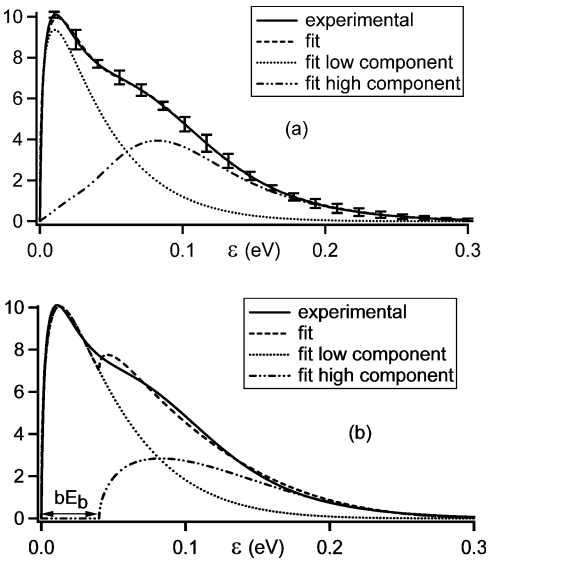

Figure 1. KERDs in the metastable window. Solid line: experimental data (with error bars). Dashed line: fit using the maximum entropy method either with three constraints for the second component (a) or with a reverse potential barrier (b). Dotted line: low kinetic energy contribution. Dashed−dotted line: higher kinetic energy contribution.

$$P(\epsilon|E) = fP^{l}(\epsilon|E) + [1 - f]P^{h}(\epsilon|E) \qquad (4.1)$$

According to a previous work of Fati et al.,[24] two models have been tested. In both cases, the low energy component, $P^l(\epsilon|E)$, is simply given by the maximum entropy method expression (eq 3.2) with a single constraint, $A_1^l(\epsilon)$. The Lagrange parameters are assumed to remain constant in the limited internal energy range sampled. The high energy contribution, $P^h(\epsilon|E)$, is expressed in a different way in both models, as explained below. The comparison of both approaches is expected to assess the robustness of our results.

The distribution $P(\epsilon|E)$ given by eq 4.1 has to be averaged over the internal energy distribution, $T(E)$ (eq 3.5). The resulting KERD is then fitted to the experimental data using a χ^2 minimization procedure. In this way, we deduce the relative weight, f, the constraints, $A_r(\epsilon)$, and the Lagrange multipliers, $\lambda_r(E)$. Very different initial values of the fitted parameters were tried in each case, and it was checked that all initial conditions converged to the same optimal set of parameters. This ensured that the global minimum of the χ^2 multidimensional surface was found.

(i) First Model: Introduction of Additional Constraints. As already mentioned, the maximum entropy expression (eq 3.2) converges to an exact distribution if the number of constraints is infinite. In this first model, we used this expression for $P^h(\epsilon|E)$ with the minimum number of constraints necessary to reach a good agreement with the experimental data. This model does not imply any assumption about the physical origin of the larger width of the high energy component.

The best fit is shown in Figure 1a. A single constraint ($A_1^l = \epsilon^{1/2}$) allows us to reproduce the narrow component of the KERD, whereas three constraints ($\epsilon^{1/2}$, ϵ, and ϵ^2) are needed to get a good quality fit for the wider component. Actually, this fit needs three constraints to convert the asymmetric prior distribution into a more or less symmetric bell-shaped distribution. Such Gaussian-like distributions have already been observed when a reverse activation barrier governs the dynamics.[24,51,52] Table 1

TABLE 1: Maximum Entropy Analysis of the KERD Recorded in the Metastable Time Window[a]

model	f	bE_b (eV)	F^l	$\langle\epsilon\rangle^l$ (eV)	F^h	$\langle\epsilon\rangle^h$ (eV)
model with three constraints	0.53		0.94	0.044	0.42	0.106
model with a barrier	0.65	0.04	0.98	0.049	0.44	0.122

[a] f is the weight of the KERD narrow component. bE_b is the amount of the reverse potential barrier directly converted into relative translational energy. F and $\langle\epsilon\rangle$ are, respectively, the ergodicity index and the average kinetic energy release at the average internal energy (E = 0.17 eV), for either the narrow component (low kinetic energy, l) or the wider component (high kinetic energy, h).

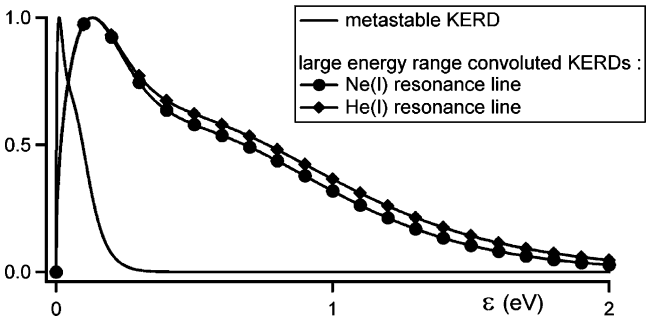

Figure 2. Comparison of the experimental KERDs obtained in the metastable window and using dissociative photoionization. To facilitate the comparison, the maximum of each distribution has been scaled to unity.

presents the parameters deduced from this fit (weight, f, ergodicity indices, and average kinetic energy release for each KERD component).

(ii) Second Model: Introduction of a Reverse Activation Barrier. The experimental distribution shows a shoulder near ϵ = 0.05 eV; that is, the influence of the second contribution is likely to begin at this kinetic energy. In addition, $P^h(\epsilon|E)$ is wider than $P^l(\epsilon|E)$. This seems to indicate a reverse barrier, E_b, from which a fraction equal to bE_b is systematically converted into translational energy.[53] We assumed therefore that the distribution $P^h(\epsilon|E)$ is shifted by bE_b toward higher kinetic energy and is given by the piece-wise defined equation

$$P^h(\epsilon|E) = \begin{cases} 0 \text{ when } \epsilon < bE_b \\ P^0(\epsilon - bE_b|E)\exp[-\lambda_0{}^h - \lambda_1{}^h A_1{}^h(\epsilon - bE_b)] \text{ when } bE_b < \epsilon < E \end{cases} \quad (4.2)$$

The fit of the experimental curve with this model is presented in Figure 1b. The best fit occurs for $A_1{}^l = \epsilon^{1/2}$ and $A_1{}^h = \epsilon^{1/2}$. We see that this model is also able to describe reasonably well the KERD. However, the quality of the fit is worse than that for the first model, because it introduces an unrealistic discontinuity. Nevertheless, the model provides an estimate of the fraction of the reverse barrier converted into translational energy, which is found to be equal to about 0.04 eV. Table 1 shows a satisfactory agreement between both models used to analyze the metastable KERD.

B. Higher Internal Energy Range. Figure 2 displays metastable data together with the non-deconvoluted KERDs obtained by dissociative photoionization with either the He(I) or Ne(I) resonance lines using the retarding field method (section IIB). As expected, much wider KERDs are obtained by photoionization compared with the metastable data because the sampled internal energy is much broader. These KERDs are also clearly bimodal and look similar. Because the low translational energy components are almost identical, they should have the same origin, whereas the high component is slightly larger for the He(I) resonance line. On the basis of previous literature data,[1−3] we made the hypothesis that the low translational energy component comes from dissociation via the ground electronic state, whereas the high translational energy component results from a fast, nonstatistical dissociation taking place on an excited electronic state. This hypothesis will be substantiated by ab initio calculations presented in section V. We now show how both contributions of the KERD could be separated.

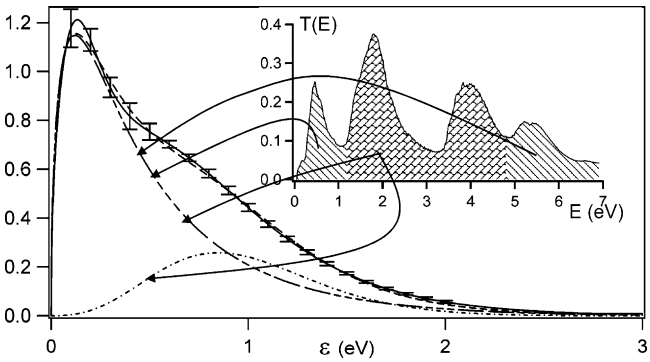

Figure 3. Non-deconvoluted KERD, $\tilde{P}^f(\epsilon)$, recorded with the He(I) resonance line, as a function of the kinetic energy released on both fragments, ϵ (see eq 2.4). Solid line: experimental data (with corresponding error bars). Dashed line: maximum entropy fit using eq 4.6 with $A_{1g} = \epsilon^{1/2}$. Dashed−dashed and dashed−dotted lines: components corresponding to, respectively, the dissociation from the ground ionic state and the fast, nonstatistical dissociation. The inset shows the corresponding internal energy distribution. The arrows indicate which energy range contributes to which part of the KERD.

We first had to decide at which internal energy the assumed nonstatistical process starts. It is clear that its onset should occur below 2.5 eV (measured from the lowest $C_2H_2F^+ + F$ dissociation asymptote), since it affects the KERD with the Ne(I) resonance line. Moreover, the breakdown curve for $C_2H_2F^+$ from 1,1-difluoroethene decreases between 0.5 and 1.15 eV and then increases again,[3,4] and an early study noticed the appearance of a structure in the KERD beyond this energy.[3] Above 4.75 eV, the breakdown curve decreases rapidly as new dissociation channels open up, leading to further H or F loss from $C_2H_2F^+$.[4] Accordingly, our model assumes that vibronic states located between 1.15 and 4.75 eV can lead either to the vibrationally excited electronic ground state via internal conversion or directly to the fragments.

The KERD is thus modeled as the sum of two contributions. The internal energy range is divided into two parts, as shown in Figure 3. The first part below 1.15 eV and above 4.75 eV corresponds to excited parent ions that rapidly convert to the ground electronic state. The second part is related to an energy range, between 1.15 and 4.75 eV, where parent ions have a probability $p(E)$ of decaying to the ground electronic state prior to dissociation and a probability $1 - p(E)$ of directly dissociating.

The KERD is then written as

$$P(\epsilon|E) = f(E)\,P_g(\epsilon|E) + [1 - f(E)]P_d(\epsilon|E) \quad (4.3)$$

where $P_g(\epsilon|E)$ and $P_d(\epsilon|E)$ respectively refer to dissociations from the electronic ground state and to direct dissociations from an excited state. The branching ratio, $f(E)$, is equal to

$$f(E) = \begin{cases} 1 \text{ when } E < 1.15 \text{ eV or } E > 4.75 \text{ eV} \\ p(E) \text{ when } 1.15 \text{ eV} < E < 4.75 \text{ eV} \end{cases} \quad (4.4)$$

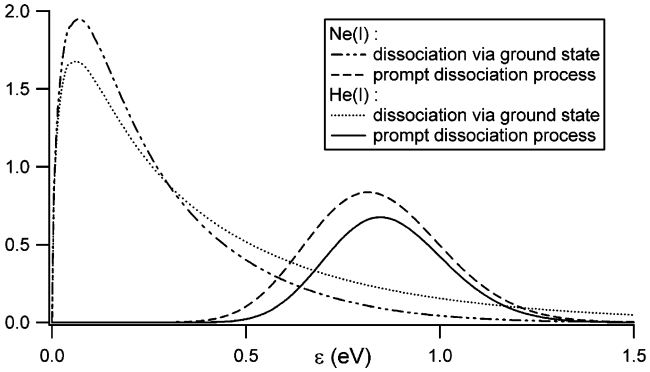

Figure 4. Deconvoluted KERDs for the dissociative photoionization experiments. This figure shows the decomposition into a statistical and a fast nonergodic component.

As usual, $P(\epsilon|E)$ must be averaged over $T(E)$ to give $\tilde{P}(\epsilon)$.

$$\tilde{P}(\epsilon) = \int_{\epsilon}^{h\nu-14.24\text{eV}} \{f(E)\, P_g(\epsilon|E) + [1 - f(E)]P_d(\epsilon|E)\}T(E)\, dE \quad (4.5)$$

$$\tilde{P}(\epsilon) = \int_{\epsilon}^{1.15\text{eV}} P_g(\epsilon|E)\, T(E)\, dE + \int_{4.75\text{eV}}^{h\nu-14.24\text{eV}} P_g(\epsilon|E)\, T(E)\, dE + \int_{1.15\text{eV}}^{4.75\text{eV}} p(E)\, P_g(\epsilon|E)\, T(E)\, dE + \int_{1.15\text{eV}}^{4.75\text{eV}} [1 - p(E)]P_d(\epsilon|E)\, T(E)\, dE \quad (4.6)$$

The first three terms represent the ground state dissociation contribution, whereas the direct, prompt dissociation is described by the fourth one. In eqs 4.5 and 4.6, $h\nu$ is the energy of the resonance line used and 14.24 eV is the appearance energy of the $C_2H_2F^+$ fragment.

$P_g(\epsilon|E)$ and $P_d(\epsilon|E)$ are given by the maximum entropy method (eq 3.2). The distribution given by eq 4.6 is then converted into a velocity distribution which is convoluted with the thermal velocity distribution (see Experiment section IIB). The resulting distribution is converted back into a KERD that can be directly compared with the un-deconvoluted experimental data. This procedure allows us to deduce the parameters of eq 4.6: $p(E)$, Lagrange multipliers, and constraints.

For the low kinetic energy component, one constraint is sufficient. The data do not allow us to decide between $\epsilon^{1/2}$ and ϵ, as already observed in the case of the pyridine ion dissociation.[28] For the high kinetic energy component, two constraints ($\epsilon^{1/2}$ and ϵ) are necessary.

Different trials have been performed: constant or linear dependence for $p(E)$ and the Lagrange multipliers, possibility of direct fragmentations in the lowest ($E < 1.15$ eV) or highest ($E > 4.75$ eV) energy ranges. All parametrizations lead to similar results so that the discussion will be based on the simplest situation with constant parameters. A typical fit to the non-deconvoluted experimental distribution is shown in Figure 3. Deconvoluted distributions are displayed in Figure 4, and the fitting parameters are summarized in Table 2. Average kinetic energy releases for the global distribution are found to be equal to 0.47 ± 0.09 and 0.53 ± 0.06 eV for, respectively, the NeI and HeI experiments. The average value of $f(E)$

$$\langle f \rangle = \int_0^{\infty} f(E)\, T(E)\, dE \quad (4.7)$$

is actually the weight of the low energy component of the KERD. The deconvolution procedure narrows the distributions and, hence, increases the intensity of each component, especially the low energy one. The relative weight of each component, however, is unaffected by the deconvolution step, as expected.

TABLE 2: Maximum Entropy Analysis of the KERDs Obtained by Dissociative Photoionization at Fixed Wavelength (Ne(I) and He(I) Resonance Lines)[a]

resonance line	$\langle E \rangle$ (eV)	constraint $A_{1g}(\epsilon)$	p	$\langle f \rangle$	F_g	$\langle \epsilon \rangle_g$ (eV)	F_d	$\langle \epsilon \rangle_d$ (eV)
Ne(I)	1.5	$\epsilon^{1/2}$	0.52	0.65	0.99	0.29	0.07	0.79
Ne(I)	1.5	ϵ	0.55	0.67	0.98	0.30	0.07	0.80
He(I)	3	$\epsilon^{1/2}$	0.61	0.74	0.99	0.41	0.22	0.89
He(I)	3	ϵ	0.61	0.74	0.99	0.41	0.21	0.92

[a] $\langle f \rangle$ represents the weight of the KERD low energy component. p is the fraction of ions in the internal energy range 1.15−4.75 eV that decay to the ground electronic state before dissociating. F and $\langle \epsilon \rangle$ are, respectively, the ergodicity index and the average kinetic energy release at the average internal energy, $\langle E \rangle$, for the narrow (g) and wide (d) components of the KERDs.

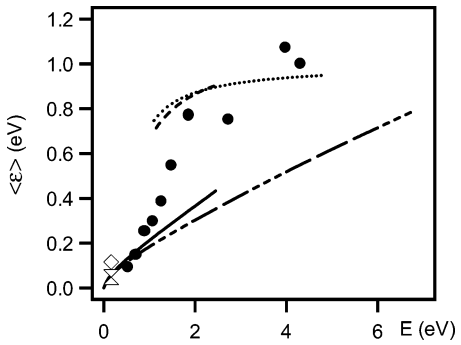

Figure 5. Average kinetic energy release as a function of internal energy (defined with respect to the lowest dissociation asymptote). Sand-glass and diamond: narrow and wide component in the metastable range. Filled circles: TPEPICO data of Güthe et al.[4] Solid and dashed−dotted lines: Ne(I) and He(I) statistical dissociations from the ground state (the displayed data correspond to $A_{1g} = \epsilon^{1/2}$). Dashed and dotted lines: Ne(I) and He(I) nonstatistical fragmentations from excited states.

Note also that the shoulder observed in the metastable KERD around 0.05 eV is not at all resolved in the dissociative photoionization experiments because of the convolution with the thermal distribution.

Figure 5 shows the average translational energy curves, $\langle \epsilon \rangle(E)$, deduced from all available distributions and from experimental data determined by Güthe et al. using a TPEPICO technique coupled with a TOF spectrometer.[4] The Ne(I) and He(I) resonance lines curves are fairly consistent. Moreover, there is good agreement between the TPEPICO data points and our curves for a dissociation process via the ground state at low energy and between the TPEPICO results and our curves for a prompt dissociation at higher energy. This is an important validation of our model, since the analytical form for $P(\epsilon|E)$ of eq 4.3 is able to account for the considerable increase of $\langle \epsilon \rangle(E)$ in the internal energy range investigated in the present and previous works. Our treatment isolates two processes, whereas the TPEPICO data provide a global measure which displays a smooth transition between the two regimes.

V. Potential Energy Surfaces

Several explanations can be a priori proposed to account for the bimodal nature of the KERDs that has been observed experimentally in both the metastable and high energy regimes. The participation of electronically excited states in the reaction mechanism, possibly as an example of "isolated state

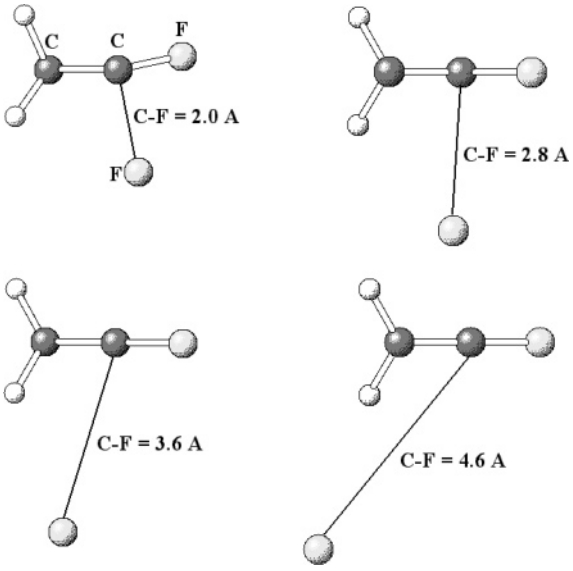

Figure 6. Optimized geometries defining the minimum energy path of the dissociating cation for selected C−F distances, in the third diabatic state, that leads to F in its $^2P_{1/2}$ state (UQCISD, 6-31G**(5d) basis set).

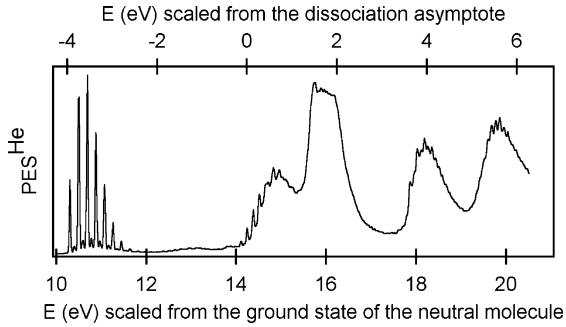

Figure 7. He(I) photoelectron spectrum of 1,1-difluoroethene.

decay",[9−18,54−57] can be postulated as a likely explanation. Electronic predissociation provides a variant of this mechanism.

As an alternative explanation, the presence of a reverse activation energy barrier along the reaction path can be envisaged. Gentry and Giese[58] have shown that the long-range interaction between a positive point charge and a fluorine atom in its $^2P_{1/2}$ state is characterized by a potential barrier of the order of 0.05 eV. Since two doublet states can be correlated with the $^2P_{3/2}$ state of the fluorine atom, this barrier occurs along the third doublet state. Ab initio calculations at various levels of sophistication have shown that the hump persists in the potential energy curve of the $\tilde{A}^2\Sigma$ state of HF^+ (0.07 eV at the QCISD(FC)/6-31G** level). However, it strongly decreases (≈0.02 eV) when the positive ion is $C_2H_2F^+$ and the shape of the energy curve in the region of large C−F distances presents some kind of a plateau. As a matter of fact, due to the overlap of their electronic clouds, the interaction between F and the cation is more complicated than a mere ion−quadrupole interaction. Consequently, the F atom and the $C_2H_2F^+$ cation can form a weak complex in a very extended region of coordinate space, as illustrated by the unexpected motion of the fluorine atom along the minimum energy path (Figure 6).

Insight into the pattern of the potential energy surfaces of the 1,1-$C_2H_2F_2^+$ molecular ion has been obtained by different techniques, highlighting different regions of configuration space.

First of all, the photoelectron spectrum[59] (Figure 7) has been reinterpreted using ab initio calculations at the equilibrium geometry of the neutral molecule, to determine the energies of the vertical transitions. The results, presented in Table 3, confirm the assignments previously proposed by Bieri et al. based on many-body Green function calculations.[60] In addition, some evidence in support of electronic predissociation can be found in the vibrational structure of the first excited state $\tilde{A}^2B_2$.

Ab initio calculations at the QCISD level were performed to determine the equilibrium geometry of the ground state and three low-lying excited electronic states as well as their respective dissociation asymptotes. The equilibrium geometries are summarized in Table 4. Note that the equilibrium CF bond length is larger in the neutral molecule than in the $\tilde{X}^2B_1$ and $\tilde{A}^2B_2$ ionic states. Moreover, the geometries of the $\tilde{B}^2A_1$ and $\tilde{D}^2A_2$ states, optimized in the C_{2v} point group, do not correspond to minima but correspond to transition states as confirmed by the negative eigenvalue of the Hessian at the MP2 level.

Getting insight into the potential energy surfaces far from the nuclear equilibrium geometries implies investigating the occurrence of surface crossings, that is, the existence of nonadiabatic interactions. Their study requires less conventional computational techniques. Crossings between potential energy surfaces can be studied by CASSCF[61] calculations. Three conical intersections have been identified using small active spaces, either CAS(3,3) or CAS(3,4), with the constraint of remaining in the C_{2v} point group. These conical intersections involved the following pairs of electronic states: ($\tilde{X}^2B_1/\tilde{A}^2B_2$), ($\tilde{A}^2B_2/\tilde{B}^2A_1$), and ($\tilde{A}^2B_2/\tilde{C}^2B_2$).

Though the nuclear geometries corresponding to the seams of these intersections are highly distorted, none of them actually correspond to a dissociating structure because all C−F bond lengths remain within a 10−15% variation range with respect to the equilibrium geometry. The search for crossings between the electronic states along the C−F dissociation pathway was then performed at the UQCISD level in a region where one of the C−F bond lengths was equal to or larger than 1.7 Å. At such geometries, the electronic density of the dissociating fluorine is clearly emerging, which greatly facilitates the convergence on the four chosen electronic states, that is, two $^2A''$ and two $^2A'$, correlating respectively with $\tilde{X}^2B_1$ and $\tilde{D}^2A_2$, on one side, and with $\tilde{B}^2A_1$ and $\tilde{C}^2B_2$ on the other side. These calculated states are in fact diabatic, since the calculation is based on a monodeterminantal zero-order wave function. In the present case, the computations reveal a crossing between the two $^2A''$ states, which would not occur between adiabatic states. Adiabatic and diabatic states are known to coincide far away

TABLE 3: Ab Initio Calculations of the Vertical Ionization Energies (eV) of 1,1-$C_2H_2F_2$ at Different Computational Levels

	$\tilde{X}^2B_1$	$\tilde{A}^2B_2$	$\tilde{B}^2A_1$	$\tilde{C}^2B_2$	$\tilde{D}^2A_2$	$\tilde{E}^2A_1$	$\tilde{F}^2B_1$	$\tilde{G}^2B_2$	$\tilde{H}^2A_1$
SAC-CI 6-31G(d)	10.16	14.79	15.53	15.74	16.08	18.33	18.31	19.88	21.82
SAC-CI 6-311G(d,p)	10.38	15.05	15.82	16.08	16.43	18.52	18.70	20.20	22.08
SAC-CI 6-311+G(d,p)	10.51	15.14	15.95	16.17	16.57	18.70	18.79	20.25	22.26
MP2	10.20	15.15	15.66		16.33				
QCISD	10.11	14.53	15.43		15.85				

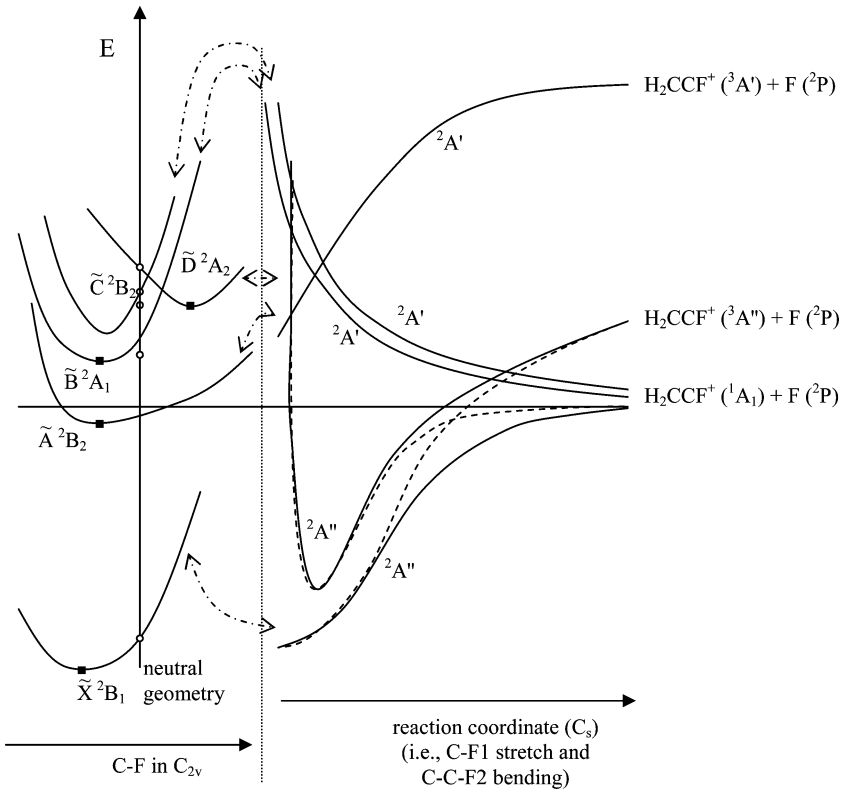

Figure 8. Scheme of the potential energy surfaces of 1,1-$C_2H_2F_2^+$ in the C_{2v} point group (left), corresponding to the initially populated Franck−Condon zone, and along the F loss dissociation coordinate (right, C_s point group). Double arrows link correlated states in both parts of the graph. The horizontal line corresponds to the energy of the lowest dissociation asymptote. The dashed lines represent the diabatic $^2A''$ states. The empty circles refer to the vertical ionization transitions, and full squares indicate the stationary points (equilibrium geometry or saddle point, depending on the electronic state).

TABLE 4: Stationary Points of the First Electronic States of 1,1-$C_2H_2F_2^+$ Detected by the ab Initio Calculations (C_{2v}, QCISD, 6-31G(5d) Basis Set)[a]**

	neutral	$\tilde{X}^2B_1$	$\tilde{A}^2B_2$	$\tilde{B}^2A_1$ (TS)	$\tilde{D}^2A_2$ (TS)
C−C (Å)	1.33	1.42	1.33	1.40	1.31
H−C (Å)	1.08	1.08	1.16	1.10	1.08
F−C (Å)	1.33	1.27	1.29	1.30	1.41
H−C−H (deg)	121	122	78	144	121
F−C−F (deg)	110	115	116	120	99

[a] They correspond to equilibrium geometries for states $\tilde{X}$ and $\tilde{A}$ and to saddle points for States $\tilde{B}$ and $\tilde{D}$.

TABLE 5: Vibrational Wavenumbers of the 1,1-Difluoroethene Cation Calculated at the MP2 Optimized Geometries in the C_{2v} Point Group[a]

	$\tilde{X}^2B_1$	$\tilde{A}^2B_2$	$\tilde{B}^2A_1$	$\tilde{D}^2A_2$
a_1	582	546	513	448*
	981*	1051*	969*	826*
	1479	1173	1158	1415
	1653*	1793	1529*	2088
	3264	2849*	3003	3258
a_2	382	893	597	844
b_1	646	336	223	643
	911	698	685	1138
b_2	419	322	i 1267	i 4304
	1039	614	606	412
	1602	1468	1262	955
	3408	2328	3197	3366

[a] The active modes in the photoelectron spectrum are denoted by an asterisk.

from a region of strong nonadiabatic coupling, but they adopt a very different behavior in the coupling area.[62−64] Adiabatic states diagonalize the electronic Hamiltonian. A meaningful calculation requires the use of a multideterminantal wave function (MCSCF, CASSCF, MRCI, ...). Diabatic states, on the other hand, are expected to remain unchanged as the coupling region is crossed. To compute them, the procedure adopted here consists of generating a QCISD potential energy curve based on a UHF calculation carried out for the electronic state under consideration.

According to these calculations, a general scheme of the potential energies of the first electronic states is presented in Figure 8 and described hereafter. Two situations are displayed. The left-hand side of the picture corresponds to C_{2v} geometry, that is, to the vicinity of the equilibrium geometry of the neutral molecule: this is appropriate to analyze the photoelectron spectrum. The right-hand side describes the situation along the reaction coordinate, in the C_s point group: this corresponds to the dissociation process. The correlation between equivalent states is shown by arrows. This figure summarizes the most salient theoretical results and will be used as a reference to interpret the experimental data. In addition, the calculated vibrational wavenumbers for the different electronic states are gathered in Table 5. We now briefly describe the key characteristics of each electronic state as well as their mutual interactions.

A. The $\tilde{X}^2B_1$ Ground Ionic State. This state correlates adiabatically with the lowest asymptote $H_2CCF^+(^1A_1)$ + F(^{2}P) but correlates diabatically with the second asymptote at 1.47 eV (above the lowest one) where the H_2CCF^+ fragment is in its $^3A''$ state. The $\tilde{D}^2A_2$ state presents the opposite behavior: it correlates adiabatically with the H_2CCF^+ fragment in its triplet state while diabatically correlating with the lowest asymptote. The equilibrium geometry of the $\tilde{X}^2B_1$ state corresponds to the C_{2v} point group. Its dissociation energy at the QCISD level is equal to 4.22 eV. The associated photoelectron band shows mainly two vibrational progressions with wavenumbers equal

to 806 and 1613 cm^{-1}. According to the geometrical changes upon ionization (see Table 4), the two normal modes corresponding to these frequencies involve several internal degrees of freedom, mainly the C−C and C−F bond lengths and the H−C−H (or H−C−C) valence angle.

B. The $\tilde{A}^2B_2$ Excited Ionic State. This state is stable and is characterized by a deep minimum in the potential energy surface. At the QCISD level, it lies 0.138 eV below the first asymptote. It correlates with the higher asymptote $C_2H_2F^+(^3A')$ + $F(^2P)$ calculated to be at 5.23 eV from the lowest one. An unexpected feature of its equilibrium conformation is the smallness of the HCH angle, equal to 78°.

The corresponding photoelectron band is characterized by an extended vibrational progression, with some irregularities that suggest nonadiabatic interactions leading to internal conversion and possibly to fast predissociations. As already mentioned, three intersections (not shown in Figure 8) involving this state were found, with the lowest one lying about 0.5 eV above the lowest dissociation asymptote and involving the fundamental state $\tilde{X}^2B_1$. The vibrational mode able to induce the electronic transition is the unique a_2 mode that corresponds to twisting the CH_2 group around the C−C bond. This intersection may be responsible for the irregularities detected in the vibrational structure of the second photoelectron band between 14.6 and 14.8 eV. The other intersections are calculated at about 1.5−2.0 eV above the asymptote and respectively involve the $\tilde{B}^2A_1$ and $\tilde{C}^2B_2$ states.

C. The $\tilde{B}^2A_1$ Excited Ionic State. No actual minimum can be detected by ab initio calculations. Within the C_{2v} point group, the calculated stationary point happens to be a saddle point. The eigenvector connecting it to the minimum belongs to the b_2 representation and distorts the system to the C_s point group. This is understandable, because the $\tilde{B}^2A_1$ state has been shown to be coupled to the $\tilde{A}^2B_2$ state and is close to $\tilde{C}^2B_2$. Thus, the stationary point is in fact a funnel (also termed a "Born−Oppenheimer hole") in the potential energy surface.

D. The $\tilde{C}^2B_2$ Excited Ionic State. The $\tilde{C}^2B_2$ state is diabatically correlated with the lowest dissociation asymptote. Its geometry and its vibrational frequencies were not calculable at the QCISD level because this state has the same symmetry as the $\tilde{A}^2B_2$ state.

E. The $\tilde{D}^2A_2$ Excited Ionic State. Within the C_{2v} point group, the stationary point obtained at the QCISD level turns out to be a saddle point. It lies at 1.603 eV above the lowest dissociation limit. The eigenvector associated with the negative value of the Hessian also belongs to the b_2 representation. The search of the minimum was done at the CAS(3,3) level and led to a structure where one of the CF bonds was equal to 1.58 Å. From a limited number of calculations at the QCISD level with a very loose convergence threshold on the UHF wave function to prevent variational collapse, it appears that the minimum could be as low as 1.6 eV under the first asymptote.

As schematically illustrated in the C_{2v} part of Figure 8, crossings between $\tilde{D}^2A_2$ and the two $\tilde{B}^2A_1$ and $\tilde{C}^2B_2$ states nearby are found for not very large C−F distances, that is, between 1.4 and 1.45 Å.

VI. Discussion

A. Metastable Internal Energy Range. *(1) Narrow Component of the KERD.* The narrow, low kinetic energy KERD component is best fitted for $\lambda_1^l A_1^l = (3.5 \pm 0.9)\epsilon^{1/2}$. The positive value of the Lagrange parameter means that the actual distribution $P^l(\epsilon|E)$ is narrower than the prior distribution $P^0(\epsilon|E)$. This observation and the nature of the constraint ($\epsilon^{1/2}$) are not unexpected for simple barrierless bond cleavage reactions.[23,43,45]

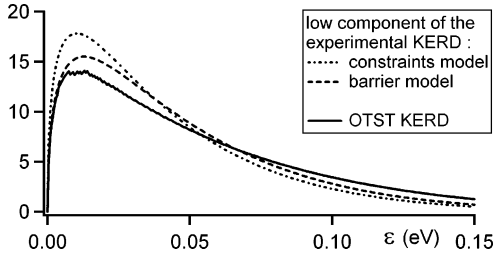

Figure 9. Narrow component of the KERD in the metastable domain: comparison between the maximum entropy fits (obtained either using additional constraints or a reverse barrier to describe the second, broader component) and the OTST prediction. The fluorine atom polarizability is taken equal to 0.557 $Å^3$,[69] the internal energy distribution is given by eq 2.1, and the total angular momentum, *J*, distribution is provided by the rotational distribution of the parent ion in the spectrometer source at 150 °C.

The ergodicity index (eq 3.4) is equal to 96 ± 2%: the mechanism that generates this part of the distribution is almost ergodic. Phase space theory in its orbiting transition state version (OTST) models KERDs for ionic barrierless dissociations at low energy.[39,50,65−68] In this theory, the combination of the rotational (*j*) and orbital (*l*) angular momenta generates dissociation channels with an *l*-dependent transition state located at the orbital potential barrier. The probability of releasing a kinetic energy, ϵ, is directly linked to the number of channels with a reverse orbital barrier smaller than ϵ.

Figure 9 shows the calculated OTST KERD together with the narrow component of the experimental KERD for both fitting models (see section IVA): there is satisfactory agreement for the first moment of the three distributions. The average OTST kinetic energy released is equal to 0.055 eV, compared to the experimental values of 0.044 and 0.049 eV (see Table 1). This agreement and the ergodicity index close to 100% suggest that the corresponding dissociation takes place along a monotonically increasing potential energy surface. This component can obviously be related to a reaction on the lowest adiabatic dissociation pathway.

(2) Large Component of the KERD. The high kinetic energy component (see Figure 1 and Table 1) is characterized by a much lower ergodicity index, of the order of 40%. The average kinetic energy release is larger than the statistical expectation, representing about 60% of the total available energy. This suggests that the dissociating ion samples repulsive parts of the potential energy surface at large interfragment separations. In other words, some kind of reverse activation barrier could be operating. The good agreement between both data handling procedures displayed in Figure 1 supports this hypothesis.

As an additional test, we applied the method developed by Zamir and Levine to analyze the origin of the fragment translational energy.[53] Assuming that the released kinetic energy originates from both the reverse barrier, E_b, and the excess nonfixed energy, $E - E_b$, and that these contributions are independent, the average kinetic energy can be expressed as

$$\langle\epsilon\rangle^h(E) = a(E - E_b) + bE_b \qquad (5.1)$$

According to the barrier model, bE_b is estimated at 0.04 eV (section IVA). The knowledge of the Lagrange multipliers, provided by the maximum entropy analysis, allows us to reconstruct an experimental $\langle\epsilon\rangle^h(E)$ curve and to fit it to eq 5.1 to find *a* and E_b. This analysis leads to $a = 0.53$ and $E_b = 0.05$ eV. For both the reverse barrier and the nonfixed contribution, a significant part of the excess energy flows into the translational degree of freedom.

A first possible explanation for the presence of a reverse activation barrier is provided by Gentry and Giese,[58] who studied the interaction between a point charge and a fluorine atom, as already discussed in section V. However, for the reaction studied here, the corresponding reverse barrier nearly disappears.

The potential energy surfaces depicted in Figure 8 suggest an alternative mechanism. As seen on the right-hand side of this figure, a nonadiabatic interaction takes place along the reaction coordinate (C_s symmetry) between the two lowest $^2A''$ ionic states. In addition, crossings with $^2A'$ states occur at larger distances. We suggest that the observed bimodal KERD reflects the competition between the adiabatic and diabatic dissociation pathways.

For the metastable dissociation, the average internal energy is 0.17 eV above the dissociation asymptote. In other words, both the $\tilde{X}^2B_1$ and the $\tilde{A}^2B_2$ states can be accessed. Internal energy conversion is, however, much more rapid than the microsecond time scale dissociation. Remember that a conical intersection involving these states has been found in C_{2v} geometry. The fragmentation process can thus be assumed to take place from the ground $\tilde{X}^2B_1$ state, which corresponds to $\tilde{X}^2A''$ in C_s symmetry. From this state, two mechanisms are possible (Figure 8). If the system follows the adiabatic pathway that directly leads to the lowest F loss asymptote, it samples a monotonically increasing potential energy surface, giving rise to the statistical narrow component discussed in the previous subsection. The diabatic pathway, on the other hand, leads to a higher-lying asymptote, not accessible with $E \approx 0.17$ eV. Interaction with the repulsive $^2A'$ states, however, may induce a transition leading eventually to the ground state fragments. When the system follows this latter pathway, it experiences a repulsive potential at long interfragment distances: this favors the release of relative translational energy. In addition, the diabatic pathway is favored by large nuclear velocity components along the reaction coordinate. This also contributes to larger kinetic energy releases than those predicted by statistics.

B. High Internal Energy Range. As explained in section IVB, we have assumed that, at low internal energy, ions relax to the ground electronic state and dissociate in the same manner as in the metastable experiment.

Beyond an energy of 1.15 eV, however, initially excited ions can either decay to the ground state by internal conversions or directly dissociate from a repulsive state. In the right-hand side of Figure 8, ab initio dissociation channels are drawn. This suggests that fast fragmentations may take place from the $\tilde{B}^2A_1$ state or from the $\tilde{C}^2B_2$ state that correlate with steeply decreasing $^2A'$ dissociation channels. We found that $43 \pm 4\%$ of the ions whose energy lies between 1.15 and 4.75 eV undergo direct dissociation ($1 - p(E)$ in Table 2).

This phenomenon is probably related to the bimodal pattern of the breakdown curve for the fluorine atom loss from ionized 1,1-difluoroethene.[3,4] The first increase of this curve is logically brought about by the rate constant increase with energy, and the first decrease is explained by the appearance of other fragments (CFH_2^+ at 0.44 eV, CF_2H^+ at 0.63 eV, and CF^+ at 0.68 eV, with respect to the F loss asympote[4]). This reflects a statistical, RRKM-like, behavior. By contrast, the second increase in the $C_2H_2F^+ + F$ breakdown curve cannot be interpreted by statistical theories: the presence of states that are repulsive along the C−F dissociation coordinate favors the loss of F compared with other channels.

As shown in Table 2 for the dissociative photoionization experiments, about 70% of the ions dissociate in a statistical way via prior internal conversion to a vibrationally hot electronic ground state. This corresponds to the low kinetic energy component of the KERD, for which the ergodicity index is very close to 100%. Note that this process is even more statistical than in the metastable range. As we already suggested in previous studies,[28,45] this could be due to the internal conversion process itself. At high energy, the system has to undergo many nonadiabatic transitions to reach the ground state, leading to a significant sampling of the phase space associated with the nuclear degrees of freedom.

During the fast, nonstatistical decay process, a substantial transfer from potential energy to translational energy occurs. However, because the CCF angle in $C_2H_2F^+$ must evolve from its initial value of 125° in the reactant region to its asymptotic value of 180° (C_{2v} geometry), the curvature in the reaction path is significant, and only a fraction of the available energy is released as kinetic energy, with the rest remaining trapped in the internal degrees of freedom of the fragments. The ergodicity index (Table 2) is very small at an average internal energy of 1.5 eV (Ne(I) experiments). It is seen to increase at higher internal energies, possibly reflecting the fact that additional electronic states become involved.

VII. Summary

Already a long time ago, the fluorine atom loss from 1,1-$C_2H_2F_2^+$ had been suggested to be a nonstatistical process. Combining the measurement of kinetic energy release distributions in two very different energy ranges with the maximum entropy method and ab initio calculations provides us with new information on the dissociation mechanism. In both kinds of experiments (metastable window with $\langle E \rangle \approx 0.2$ eV and dissociative photoionization with $\langle E \rangle \geq 1.5$ eV), the KERDs are bimodal, suggesting that two mechanisms are involved. Altogether, the proposed explanations for this behavior in both internal energy regimes are consistent with each other.

The first component is due to a statistical adiabatic reaction from the ground ionic state of 1,1-$C_2H_2F_2^+$, $\tilde{X}^2B_1$. This state is adiabatically correlated with the lowest dissociation asymptote, $H_2CCF^+(^1A_1) + F(^2P)$. Dissociations taking place along this adiabatic channel give rise to a narrow KERD component corresponding to low kinetic energies. They display the usual properties of a simple bond cleavage KERD, in particular, a statistical sampling, close to 100%, of the available phase space.

The $\tilde{X}^2B_1$ state is also diabatically correlated with an excited state of the fragments. A diabatic dissociation pathway from this state crosses the repulsive $\tilde{B}^2A_1$ and $\tilde{C}^2B_2$ states ($^2A'$ in C_s symmetry) during the fragment receding motion. This channel is suggested to be responsible for the second component observed on the microsecond time scale. This process is favored by larger nuclear velocities along the reaction coordinate and is therefore nonstatistical with an ergodicity index close to 40%.

In the photoionization experiments, the second and third excited electronic states $\tilde{B}^2A_1$ and $\tilde{C}^2B_2$ are reached in the Franck−Condon zone about 1.75 eV above the lowest dissociation asymptote, but they are correlated with the latter at large interfragment distances. They are therefore repulsive along the dissociation coordinate (C_s symmetry). The broad, bell-shaped, high kinetic energy component of the KERD recorded under dissociative photoionization conditions results from a direct dissociation from these states, prior to energy randomization, that is, from a conversion of potential into relative translational energy of the fragments.

As can be seen from Figure 3 and from the data of Table 2, the internal energy distributions accessed by our experiments cover mainly the 0−5 eV range (measured with respect to the $C_2H_2F^+ + F$ dissociation asymptote). This corresponds, in

TPEPICO experiments, to a photon energy lower than 19 eV. Our analysis is thus basically limited to this internal energy domain. Larger internal energies are sampled with lower probabilities. In other words, our work does not provide us with information about consecutive reactions that take place above 19 eV [4] and are therefore not expected to play an important role under our experimental conditions.

Acknowledgment. E.G. is grateful to Dr D. Fati for many fruitful discussions. This work has been supported by the "Actions de Recherche Concertée (ARC)" (Convention 99/04-245, Direction de la Recherche Scientifique−Communauté Française de Belgique) and the F.N.R.S. (Belgium). D.D.'s contribution was supported by the Belgian 'Programme des Pôles d'Attraction Interuniversitaire' (PAI n° P4/03) initiated by the Belgian State, Prime Minister's Office, Federal Office of Scientific, Technical and Cultural Affairs.

References and Notes

(1) Lifshitz, C.; Long, F. A. *J. Phys. Chem.* **1965**, *69*, 3737.
(2) Reinke, D.; Kraessig, R.; Baumgärtel, H. *Z. Naturforsch., A: Phys. Sci.* **1973**, *28*, 1021.
(3) Frey, R. *Doktorarbeit*, Universität Freiburg-in-Breisgau, 1974.
(4) Güthe, F.; Locht, R.; Leyh, B.; Baumgärtel, H.; Weitzel, K. M. *J. Phys. Chem. A* **1999**, *103*, 8404.
(5) Jochims, H. W.; Lohr, W.; Baumgärtel, H. *Nouv. J. Chim.* **1979**, *3*, 109.
(6) Frenking, G.; Koch, W.; Schaale, M.; Baumgärtel, H. *Int. J. Mass Spectrom. Ion Phys.* **1984**, *61*, 305.
(7) Stadelmann, J. P.; Vogt, J. *Adv. Mass Spectrom.* **1980**, *8A*, 47.
(8) Stadelmann, J. P.; Vogt, J. *Int. J. Mass Spectrom. Ion Phys.* **1980**, *35*, 83.
(9) Roorda, M.; Lorquet, A. J.; Lorquet, J. C. *J. Phys. Chem.* **1991**, *95*, 9118.
(10) Momigny, J.; Locht, R. *Chem. Phys. Lett.* **1993**, *211*, 161.
(11) Dannacher, J.; Schmelzer, A.; Stadelmann, J. P.; Vogt, J. *Int. J. Mass Spectrom. Ion Phys.* **1979**, *31*, 175.
(12) Creasey, J. C.; Smith, D. M.; Tuckett, R. P.; Yoxall, K. R.; Codling, K.; Hatherly, P. A. *J. Phys. Chem.* **1996**, *100*, 4350.
(13) Powis, I. *Mol. Phys.* **1980**, *39*, 311.
(14) Jarvis, G. K.; Boyle, K. J.; Mayhew, C. A.; Tuckett, R. P. *J. Phys. Chem. A* **1998**, *102*, 3219.
(15) Inghram, M. G.; Hanson, G. R.; Stockbauer, R. *Int. J. Mass Spectrom. Ion Phys.* **1980**, *33*, 253.
(16) Simm, I. G.; Danby, C. J.; Eland, J. H. D. *Int. J. Mass Spectrom. Ion Phys.* **1974**, *14*, 285.
(17) Eland, J. H. D.; Frey, R.; Kuestler, A.; Schulte, H.; Brehm, B. *Int. J. Mass Spectrom. Ion Phys.* **1976**, *22*, 155.
(18) Weitzel, K.-M.; Güthe, F.; Mähnert, J.; Locht, R.; Baumgärtel, H. *Chem. Phys.* **1995**, *201*, 287.
(19) Brehm, B.; Frey, R.; Kuestler, A.; Eland, J. H. D. *Int. J. Mass Spectrom. Ion Phys.* **1974**, *13*, 251.
(20) Levine, R. D.; Kinsey, J. L. In *Atom-Molecule Collision Theory. A Guide for the Experimentalist*; Bernstein, R. B., Ed.; Plenum: New York, 1979.
(21) Levine, R. D.; Bernstein, R. B. In *Dynamics of Molecular Collisions*; Miller, W. H., Ed.; Plenum: New York, 1976; Part B.
(22) Lias, S. G.; Bartmess, J. E.; Liebman, J. F.; Holmes, J. L.; Levin, R. D.; Mallard, W. G. *J. Phys. Chem. Ref. Data* **1988**, *17* (1).
(23) Urbain, P.; Leyh, B.; Remacle, F.; Lorquet, A. J.; Flammang, R.; Lorquet, J. C. *J. Chem. Phys.* **1999**, *110*, 2911.
(24) Fati, D.; Lorquet, A. J.; Locht, R.; Lorquet, J. C.; Leyh, B. *J. Phys. Chem. A* **2004**, *108*, 9777.
(25) Locht, R. *Int. J. Mass Spectrom. Ion Processes* **1995**, *148*, L17.
(26) Servais, C.; Locht, R. *Chem. Phys. Lett.* **1995**, *236*, 96.
(27) Hoxha, A.; Leyh, B.; Locht, R. *Rapid Commun. Mass Spectrom.* **1999**, *13*, 275.
(28) Gridelet, E.; Locht, R.; Lorquet, A. J.; Lorquet, J. C.; Leyh, B. *Int. J. Mass Spectrom.* **2003**, *228*, 389.
(29) Barber, M.; Elliot, R. M. Proceedings of the 12th Annual Conference on Mass Spectrometry, Montreal, ASTM E-14, 1964.
(30) Jennings, K. R. *J. Chem. Phys.* **1965**, *43*, 4176.
(31) Barber, M.; Green, B. N.; Wolstenholme, W. A.; Jennings, K. R. *Adv. Mass Spectrom.* **1968**, *4*, 89.
(32) Holmes, J. L.; Osborne, A. D. *Int. J. Mass Spectrom. Ion Phys.* **1977**, *23*, 189.
(33) Cooks, R. G.; Beynon, J. H.; Caprioli, R. M.; Lester, G. R. *Metastable Ions*; Elsevier: Amsterdam, The Netherlands, 1973.
(34) Beynon, J. H.; Fontaine, A. E.; Lester, G. R. *Int. J. Mass Spectrom. Ion Phys.* **1972**, *8*, 341.
(35) Szilagyi, Z.; Vekey, K. *Eur. Mass Spectrom.* **1995**, *1*, 507.
(36) Rumpf, B. A.; Derrick, P. J. *Int. J. Mass Spectrom. Ion Processes* **1988**, *82*, 239.
(37) Yeh, I. C.; Kim, M. S. *Rapid Commun. Mass Spectrom.* **1992**, *6*, 115.
(38) Güthe, F.; Baumgärtel, H.; Weitzel, K. M. *J. Phys. Chem. A* **2001**, *105*, 7508.
(39) Baer, T.; Hase, W. L. *Unimolecular Reaction Dynamics. Theory and Experiments*; Oxford University Press: New York, 1996.
(40) Levine, R. D. *Adv. Chem. Phys.* **1981**, *47*, 239.
(41) Levine, R. D.; Bernstein, R. B. *Molecular Reaction Dynamics and Chemical Reactivity*; Oxford University: New York, 1987.
(42) Alhassid, Y.; Levine, R. D. *J. Chem. Phys.* **1977**, *67*, 4321.
(43) Urbain, P.; Remacle, F.; Leyh, B.; Lorquet, J. C. *J. Phys. Chem.* **1996**, *100*, 8003.
(44) Urbain, P.; Leyh, B.; Remacle, F.; Lorquet, J. C. *Int. J. Mass Spectrom.* **1999**, *185*−*187*, 155.
(45) Hoxha, A.; Locht, R.; Lorquet, A. J.; Lorquet, J. C.; Leyh, B. *J. Chem. Phys.* **1999**, *111*, 9259.
(46) Iachello, F.; Levine, R. D. *Europhys. Lett.* **1987**, *4*, 389.
(47) Frisch, M. J.; Trucks, G. W.; Schlegel, H. B.; Scuseria, G. E.; Robb, M. A.; Cheeseman, J. R.; Zakrzewski, V. G.; Montgomery, J. A., Jr.; Stratmann, R. E.; Burant, J. C.; Dapprich, S.; Millam, J. M.; Daniels, A. D.; Kudin, K. N.; Strain, M. C.; Farkas, O.; Tomasi, J.; Barone, V.; Cossi, M.; Cammi, R.; Mennucci, B.; Pomelli, C.; Adamo, C.; Clifford, S.; Ochterski, J.; Petersson, G. A.; Ayala, P. Y.; Cui, Q.; Morokuma, K.; Malick, D. K.; Rabuck, A. D.; Raghavachari, K.; Foresman, J. B.; Cioslowski, J.; Ortiz, J. V.; Baboul, A. G.; Stefanov, B. B.; Liu, G.; Liashenko, A.; Piskorz, P.; Komaromi, I.; Gomperts, R.; Martin, R. L.; Fox, D. J.; Keith, T.; Al-Laham, M. A.; Peng, C. Y.; Nanayakkara, A.; Gonzalez, C.; Challacombe, M.; Gill, P. M. W.; Johnson, B.; Chen, W.; Wong, M. W.; Andres, J. L.; Gonzalez, C.; Head-Gordon, M.; Replogle, E. S.; Pople, J. A. *Gaussian 98*, revision A.7; Gaussian, Inc.: Pittsburgh, PA, 1998.
(48) Jensen, F. *Introduction to computational chemistry*; Wiley: New York, 1999.
(49) Scott, A. P.; Radom, L. *J. Phys. Chem.* **1996**, *100*, 16502.
(50) Gilbert, R. G.; Smith, S. C. *Theory of Unimolecular and Recombination Reactions*; Blackwell Scientific Publications: Oxford, U.K., 1990.
(51) Lee, T. G.; Park, S. C.; Kim, M. S. *J. Chem. Phys.* **1996**, *104*, 4517.
(52) Choi, T. H.; Park, S. T.; Kim, M. S. *J. Chem. Phys.* **2001**, *114*, 6051.
(53) Zamir, E.; Levine, R. D. *Chem. Phys.* **1980**, *52*, 253.
(54) Lorquet, J. C. In *The Structure, Energetics and Dynamics of Organic Ions*; Baer, T., Ng, C. Y., Powis, I., Eds.; Wiley: Chichester, U.K., 1996; p 167.
(55) Galloy, C.; Lecomte, C.; Lorquet, J. C. *J. Chem. Phys.* **1982**, *77*, 4522.
(56) Lane, I. C.; Powis, I. *J. Phys. Chem.* **1993**, *97*, 5803.
(57) Hatherly, P. A.; Smith, D. M.; Tuckett, R. P. *Z. Phys. Chem. (Muenchen)* **1996**, *195*, 97.
(58) Gentry, W. R.; Giese, C. F. *J. Chem. Phys.* **1977**, *67*, 2355.
(59) Locht, R.; Leyh, B. Unpublished results.
(60) Bieri, G.; Von Niessen, W.; Aasbrink, L.; Svensson, A. *Chem. Phys.* **1981**, *60*, 61.
(61) (a) Hegarty, D.; Robb, M. A. *Mol. Phys.* **1979**, *38*, 1795. (b) Eade, R. H. E.; Robb, M. A. *Chem. Phys. Lett.* **1981**, *83*, 362. (c) Bernardi, F.; Bottini, A.; McDougall, J. J. W.; Robb, M. A.; Schlegel, H. B. *Faraday Symp. Chem. Soc.* **1984**, *19*, 137.
(62) Nakamura, H. *Nonadiabatic Transition. Concepts, Basic Theories and Applications*; World Scientific: Singapore, 2002.
(63) (a) Yarkony, D. R. In *Conical Intersections. Electronic Structure, Dynamics and Spectroscopy*; Domcke, W., Yarkony, D. R., Köppel, H., Eds.; Advanced Series in Chemical Physics; World Scientific: Singapore, 2004; p 129. (b) Köppel, H. In *Conical Intersections. Electronic Structure, Dynamics and Spectroscopy*; Domcke, W., Yarkony, D. R., Köppel, H., Eds.; Advanced Series in Chemical Physics; World Scientific: Singapore, 2004; p 175.
(64) Lorquet, J. C.; Leyh, B. Nonadiabatic reactions. In *The Encyclopedia of Mass Spectrometry*; Armentrout, P. B., Ed.; Elsevier: Amsterdam, The Netherlands, 2003; Vol. 1, p 33.
(65) Leyh, B.; Lorquet, J. C. Kinetic energy release distributions in mass spectrometry. In *The Encyclopedia of Mass Spectrometry*; Armentrout, P. B., Ed.; Elsevier: Amsterdam, The Netherlands, 2003; Vol. 1, p 17.
(66) Forst W. *Unimolecular reactions. A concise introduction*; Cambridge University Press: Cambridge, U.K., 2003.
(67) Chesnavich, W. J.; Bowers, M. T. *J. Chem. Phys.* **1977**, *66*, 2306.
(68) Gridelet, E.; Lorquet, J. C.; Leyh, B. *J. Chem. Phys.* **2005**, *122*, 094106/1-14.
(69) Miller, T. M.; Bederson, B. *Adv. At. Mol. Phys.* **1977**, *13*, 1.